OPEN

Monodisperse Porous Silicon Spheres as Anode Materials for Lithium Ion Batteries

Wei Wang[1], Zachary Favors[1], Robert Ionescu[2], Rachel Ye[1], Hamed Hosseini Bay[1], Mihrimah Ozkan[2] & Cengiz S. Ozkan[1]

[1]Materials Science and Engineering Program, Department of Mechanical Engineering, Department of Electrical Engineering, University of California, Riverside, CA 92521 (USA), [2]Department of Electrical Engineering, Department of Chemistry, University of California, Riverside, CA 92521 (USA).

Highly monodisperse porous silicon nanospheres (MPSSs) are synthesized via a simple and scalable hydrolysis process with subsequent surface-protected magnesiothermic reduction. The spherical nature of the MPSSs allows for a homogenous stress-strain distribution within the structure during lithiation and delithiation, which dramatically improves the electrochemical stability. To fully extract the real performance of the MPSSs, carbon nanotubes (CNTs) were added to enhance the electronic conductivity within the composite electrode structure, which has been verified to be an effective way to improve the rate and cycling performance of anodes based on nano-Si. The Li-ion battery (LIB) anodes based on MPSSs demonstrate a high reversible capacity of 3105 mAh g^{-1}. In particular, reversible Li storage capacities above 1500 mAh g^{-1} were maintained after 500 cycles at a high rate of C/2. We believe this innovative approach for synthesizing porous Si-based LIB anode materials by using surface-protected magnesiothermic reduction can be readily applied to other types of SiO$_x$ nano/microstructures.

Faster, lighter, smaller, more powerful and reliable battery devices are needed for the development of portable electronics, electrical vehicles (EVs), and renewable energy resources[1–7]. Among all types of batteries, LIBs demonstrate better safety performance compared to other types of battery systems including Li metal batteries. Moreover, LIBs possess a balanced large volumetric energy density (Wh L^{-1}) and gravimetric energy density (Wh kg^{-1}) simultaneously. Compared with the conventionally used anode material, graphite, which has a limited capacity ~372 mAh g^{-1} (due to the stoichiometric limit of Li-ion intercalation in LiC$_6$), silicon is considered to be the candidate anode material for future LIBs due to its high theoretical capacity of 4200 mAh g^{-1} (corresponding to Li$_{22}$Si$_5$) and low discharge potential. Silicon is one of the rock forming elements and is the second most abundant element in earth's crust. Applying silicon based anodes to LIBs is considered a feasible route to make more powerful batteries with lower weight, smaller volume and lower cost[8–10]. However, silicon is easily pulverized and has very poor capacity retention due to its large volume change (~300%) during alloying and dealloying with lithium. In addition, the unstable solid electrolyte interface (SEI) layer and poor electron conductivity of silicon hinder the application of Si-based anodes in real LIB devices[1,11].

To solve the aforementioned problems, significant research efforts have been focused on optimizing Si-based LIB anodes. Downsizing the dimensions of silicon structures has been proven to be an effective way of avoiding pulverization for both crystalline and amorphous forms of silicon[12,13]. Extensive research has been conducted on nanostructured silicon such as silicon nanoparticles[14], silicon nanotubes/nanowires[1,15], silicon thin films, and 3D porous structures[16,17]. In addition, porous doped silicon nanowires and nanoparticles demonstrate stable cycling due to a large electrolyte-accessible surface area, short Li-ion diffusion length, and high electron conductivity[11,18]. However, the aforementioned porous silicon nanostructures are mostly produced via wet etching of single crystal silicon wafers, chemical doping, or chemical vapor deposition, all of which require very expensive starting materials or high processing costs.

In this work, we report on the synthesis of highly monodisperse porous silicon nanospheres (MPSSs) via a simple and scalable hydrolysis process with subsequent surface-protected magnesiothermic reduction. The monodisperse and spherical nature of the MPSSs allows for a homogeneous stress-strain distribution within the structure during lithiation and delithiation, which dramatically improves the electrochemical stability. The high porosity offers a large electrolyte accessible surface area, short Li-ion diffusion length, and void spaces necessary for volume expansion. The LIB anodes based on MPSSs demonstrate a very high reversible capacity of 3105 mAh g^{-1}, and minimal capacity fading was observed over 500 cycles at high rate of C/2 (80% capacity
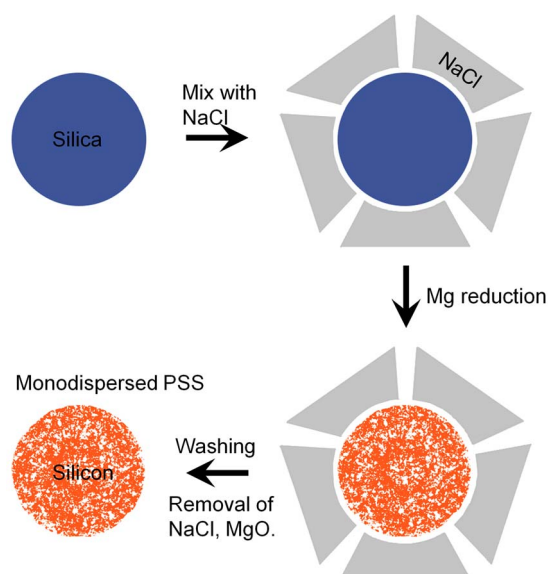
Figure 1 | Illustration of monodisperse porous silicon sphere formation through surface-protected magnesiothermic reduction.

retention with 100% Coulombic efficiency). We believe this innovative, high-throughput, and low-cost approach for synthesizing monodisperse and porous silicon-based LIB anode materials by using surface-protected magnesiothermic reduction can be readily applied to other types of SiO_x nanostructures.

Results

Silicon materials are obtained via thermic reduction of silica materials which can be achieved via a few well-studied mechanisms such as carbothermic, calciothermic, aluminothermic, and magnesiothermic reductions. Magnesiothermic reduction has garnered significant attention due to its relatively lower processing temperature ~650°C compared with >2000°C (carbothermic). The detailed schematic illustration of the synthesis process of MPSSs is shown in Fig. 1.

Gram-level monodisperse solid silica spheres (SSs) were prepared via a modified Stober method[19]. The diameter of the as-prepared SSs varies from 0.05 μm to 2 μm, and the diameter used in this work is ~200 nm. In order to preserve the diameter and shape of the nanospheres, sodium chloride (NaCl) was introduced as an effective heat scavenger which can halt the reaction temperature rise at 801°C during fusion and aid in preserving the nanosphere morphology[8,20]. MSSSs are firstly mechanically milled in an alumina mortar to reduce agglomerations and then ground together with sodium chloride (NaCl, >99.5%, Fisher Scientific) in a $1:10$ SiO_2:NaCl w/w ratio. The as-prepared SiO_2:NaCl powder is immersed in DI H_2O and ultrasonicated for 1 hour and subsequently vigorously stirred at 50°C for 3 hours. The solution is then dried at 105°C overnight under vacuum to remove all water. The dried SiO_2:NaCl powder is reground briefly to pulverize large NaCl crystals produced during drying and is then mixed with Mg (99.5%, −325 mesh, Sigma-Aldrich) in a $1:0.9$ w/w SiO_2:Mg ratio. After vortexing the powder for ample mixing, the powder is loaded into SS 316 Swagelok-type reactors in an Ar-filled VAC Omni-lab glovebox (0.5 ppm H_2O, <0.1 ppm O_2). The reactors are loaded into an MTI GSL-1200X quartz tube furnace and purged with Ar. The furnace is heated to 700°C at a rate of 5°C/min, held for 6 hours, and cooled to room temperature. The resulting product is then washed with DI H_2O several times to remove NaCl. Unwanted Mg_2Si and MgO is removed via etching in 2 M HCl overnight with subsequent washing with DI H_2O. Unreacted SiO_2 is removed by etching in 5% HF for 1 hour. The powder is rinsed several times with DI H_2O, dispersed in ethanol, and ultimately dried under vacuum for 4 hours at 105°C.

Powder X-ray diffraction (XRD) measurements were performed to characterize the phase and purity of the as-prepared SSs and MPSSs in Fig. 2a. The black spectra and red spectra can be indexed as silica and polycrystalline silicon which are associated with SSs and MPSSs, respectively. The narrow and sharp XRD peaks, without obvious amorphous scattering, exhibited by MPSSs suggest a high degree of crystallinity and they can be indexed to a cubic phase of silicon. Raman spectroscopy was used to further examine the as obtained SSs and MPSSs material. The sharp peak at a shift of 521.1 cm^{-1} for the red spectra is in good agreement with Si.
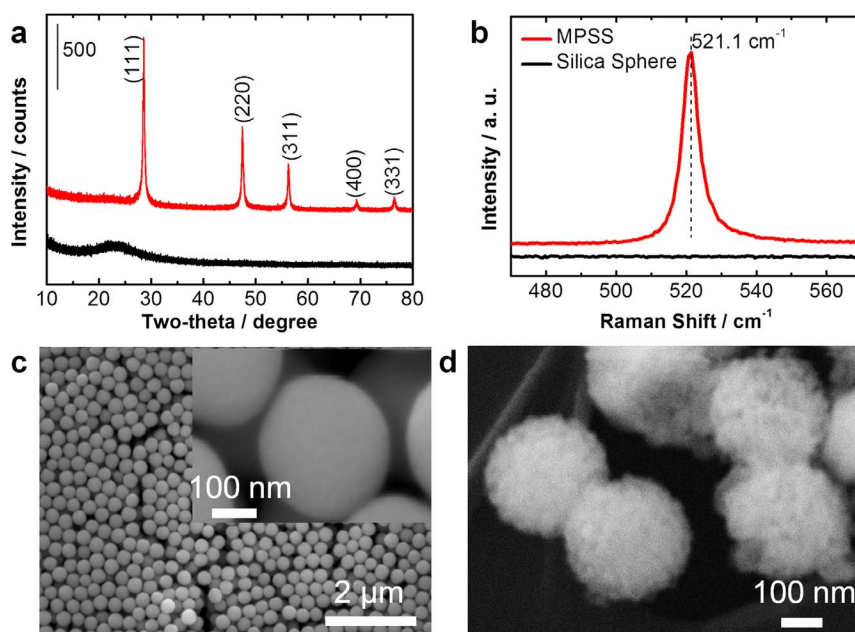

Figure 2 | (a) XRD patterns and (b) Raman spectra of monodisperse solid silica spheres and monodisperse porous silicon spheres. (c) SEM micrographs of monodisperse solid silica spheres, inset shows the high magnification SEM micrograph of the silica sphere. (d) SEM micrograph of monodisperse porous silicon spheres.

Scanning electron microscopy (SEM) micrographs are shown to illustrate the structural and morphological information of the as-synthesized SSs and MPSSs Fig. 2c and 2d. Both SSs and MPSSs possess a diameter ~200 nm. Before reduction, SSs assume a monodisperse and solid sphere nature, but after reduction the MPSSs have obtained substantial porosity while maintaining the original spherical morphology. The morphology of as prepared SSs and MPSSs was further examined in a CM300 transmission electron microscope at an accelerating voltage of 300 kV, as in Fig. 3a–d. Fig. 1a and 1b confirm an obvious transition from a monodisperse solid silica sphere to monodisperse porous silicon sphere while preserving the same size and shape after reduction. The MPSS crystals are highly porous with a pore size in the mesopore range. High resolution TEM (HRTEM) confirms the highly crystalline nature of the MPSS sample, with a d-spacing of 0.32 nm, as in Fig. 3d. The Langmuir and Brunauer-Emmett-Teller (BET) surface areas of SSs were measured to be 20.07 and 11.89 m^2 g^{-1}, respectively, and the pore distribution suggests the as-prepared SSs have limited surface area and porosity. However, a nearly 20 times enlargement of surface area (Langmuir: 353.22, BET: 214.65 m^2 g^{-1}) is achieved by MPSSs, as in Fig. 4a. The pore distribution suggests the high surface area of MPSSs is due to a combination of mesopores and micropores. Previous works suggest porous silicon with high porosity can maintain its structure during lithiation and delithiation while having relatively low stress compare with bulk form Si which is beneficial for achieving high capacity and long cycling life[8,18].

LIB 2032-type half cells were fabricated in an Ar-filled glove box (O_2 < 0.10 ppm, H_2O < 0.5 ppm) with SS and MPSS electrode as the anode and pure Li metal as the counter electrode. The electrodes were prepared by casting a slurry containing 70% active material (MPSS or SS in this work), 20% conductive additive (carbon black/carbon black with 2 wt.% CNTs), and 10% alginate which has been verified to be an effective binder system for nano-Si and porous Si[18,21]. 2 wt.% CNTs was added to the electrode slurry to improve the rate performance and to fully extract the real performance of the MPSS materials in this work. A porous PP membrane (Celgard 3501) was used as the separator. In this work, 1 M $LiPF_6$ dissolved in a 1 : 1 (v : v) mixture of ethylene carbonate (EC) and dimethyl carbonate (DMC) was used as the electrolyte. Cyclic voltammetry (CV) was performed with a voltage window range of 0.01 to 2.0 V (vs. Li^+/Li) at a scan rate of 0.2 mV sec^{-1}. Galvanostatic charge-discharge and cycling performance measurements were conducted at a fixed voltage window between 0.01 V and 2.0 V (vs. Li^+/Li). Silicon oxide materials have been previously proven to be electrochemically active based on following reactions **Eq. 1–3**[22,23].

$$SiO_x + yLi + ye \leftrightarrow Si + Li_yO_x \qquad (1)$$

$$SiO_x + yLi \leftrightarrow Li_ySiO_x \qquad (2)$$

$$Si + Li + xe \leftrightarrow Li_xSi \qquad (3)$$

Fig. 4a and Fig. S1 show the 2nd cycle cyclic voltammogram of the MPSS and SS electrodes at a scan rate of 0.2 mV sec^{-1}. CV plot during the charge of the SS electrode shows a noticeable peak < 0.33 V which can be attributed to the alloying while two other minor noticeable peaks at the higher potential (0.55 V and 1.4 V) are due to the irreversible reaction between electrode and electrolyte[22,23]. The peak in the potential of 0.25 V during the discharge of the SS electrode is due to the dealloying. The current response of SS electrode is much lower compare with MPSS electrode. We believe this can be due to two reasons. (i) Silica has smaller capacity compare with silicon. (ii) the solid nature of SSs suggests the SSs have limited electrolyte accessible surface area compare with MPSS which has been verified by the BET measurement shown in Figure 3e. The reduction peak of the MPSS electrode observed during charge process is associated with the alloying of Li-Si(<0.33 V) while the two broad peaks during discharge are from delithiation of amorphous lithium silicide (a-Li_xSi, x ~ 3.75)[1,24]. The charge-discharge voltage profiles are in good agreement with the CV measurements. Fig. 4b shows the LIB with a MPSS electrode tested at a current density of C/20 with a voltage range between 0.01 V and 2.0 V, which can be considered as deep charging and discharging for the first three cycles. The MPSS electrode exhibits a reversible discharge capacity of 3105 mAh g^{-1} from the 1st cycle (after 1st discharge). After the 1st charge, the current-potential characteristics become approximately consistent for subsequent cycles. This capacity faded slightly during the following cycles (2nd cycle: 2980 mAh g^{-1}, 3rd cycle: 2930 mAh g^{-1}). After 50 charge-discharge cycles at relatively low rate of C/20 the capacitance level is still >2200 mAh g^{-1}. The columbic efficiency obtained for all cycles from the second cycle onward is around 100%, suggesting a very good reversibility for MPSS electrodes which is superior to previously reported silica based anodes and comparable with previously published silicon-based anode systems. The irreversible discharge capacity for the first charge is due to the formation of the SEI layer on the surface of MPSS electrodes[25]. Fig. 4d shows the rate performance of the MPSS anodes with and without a 2 wt.% CNT addition. With the increase of charge-discharge current density from C/20 to 2C, capacities of the MPSS-CNT anodes decrease from
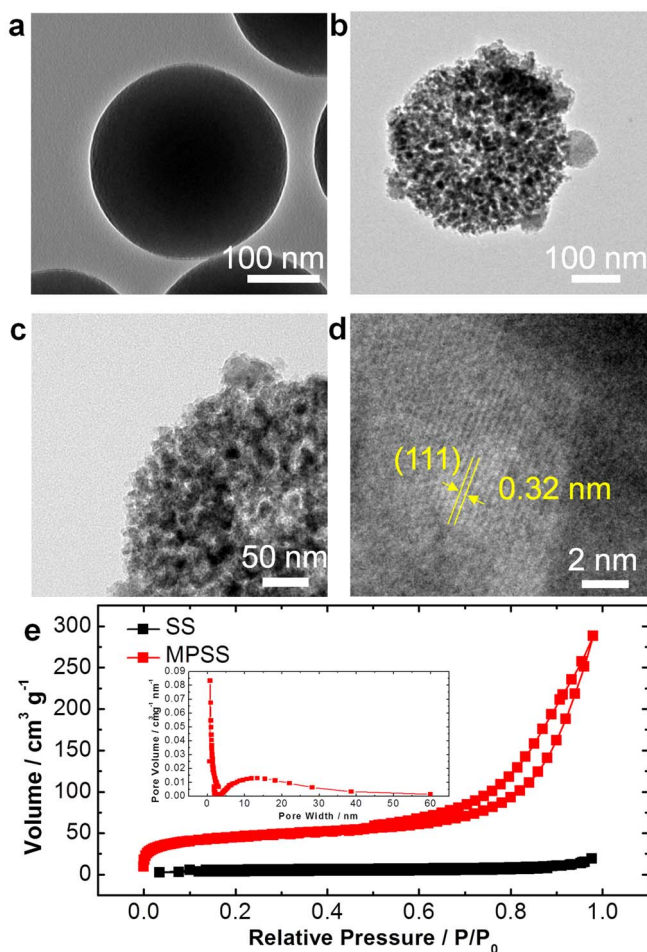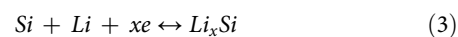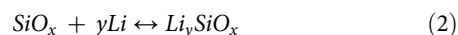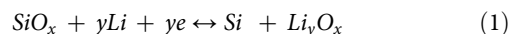

Figure 3 | TEM images of (a) monodisperse solid silica spheres (SS) and (b–d) monodisperse porous silicon spheres (MPSS), respectively. (e) BET surface area measurements of SSs and MPSSs with type IV N_2 adsorption and desorption isotherms. Inset shows the pore size distribution of MPSSs.
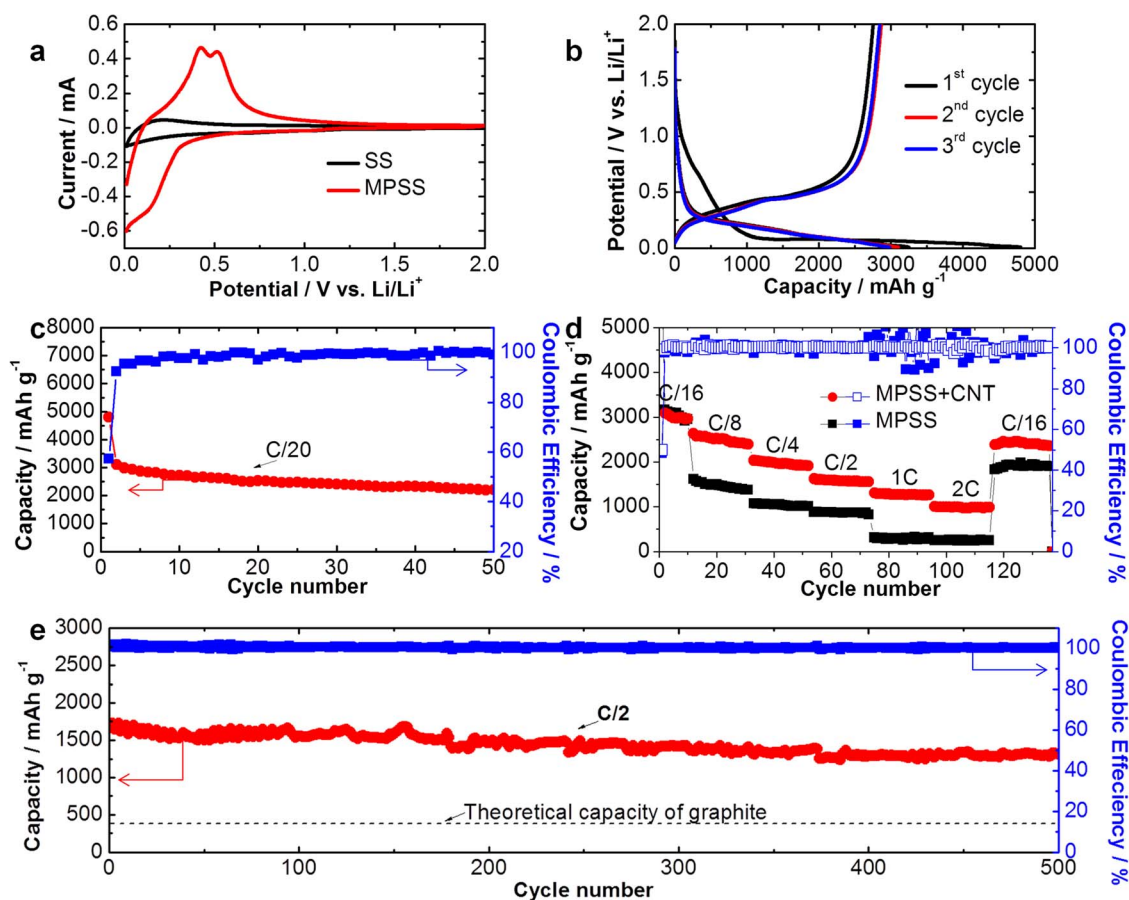
Figure 4 | (a) Cyclic voltammetry characteristic of the SS and MPSS based LIB anodes. Scan rate: 0.2 mV sec-1. (b–c) Galvanostatic charge-discharge profiles, cycling performance and coulombic efficiency of the MPSS electrodes (with 2 wt% CNT additive) at a current density of C/20. (d) High-rate cycling performance of the LIB with MPSS electrodes with CNTs and with and without CNTs. (e) Cycling performance and Coulombic efficiency of MPSS electrodes at a higher current density of C/2.

~3000 mAh g^{-1} to ~1000 mAh g^{-1}, while MPSS-carbon black anodes drop to ~260 mAh g^{-1}. MPSS anodes without CNTs show very low capacity and poor Columbic efficiency at high rates (1C or 2C), as in Fig. 4d. This is due to insufficient charge transfer provided by the micrometer level carbon black within the MPSS anode. Adding a certain amount of CNTs has been verified to be an effective way to improve the rate performance and cycling stability without changing the active materials ratio, as in Fig. 4d. The battery also shows good reversibility after being discharged at higher rate of C/2, seen in Fig. 4e. Excellent capacity retention (>80%) over 500 cycles and nearly 100% Coulombic efficiency suggests MPSS anodes have very good stability and reversibility. It is encouraging to see that a reversible capacity of >1500 mAh g^{-1} is achieved under a current density of C/2 which is much higher when compared with conventionally used graphite-based anodes.

Discussion

Since the MPSSs used in this work are ~200 nm in diameter, conventionally used micrometer-sized carbon blck is not adequate to facilitate charge transfer within the electrode while maintaining a reasonable active material ratio. We believe the addtion of CNTs helps to extract the real performance of the MPSSs by improving charge transfer and interface electronic contact resistance. This effectiveness of this hypothesis has been verified by the enhanced rate performance shown in Fig. 4d. To further verify this hypothesis and study the detailed mechanism, electrochemical impedance spectroscopy (EIS) tests were performed on MPSS based anodes with carbon black only and carbon black together with a 2 wt.% CNT conductive

additive. The typical Nyquist plots consist of two semicircles and one linear diffusion drift are shown in Fig. 5a–c. The high frequency intercept, commonly interpreted as equivalent series resistance (*ESR* or R_S), relates to the ohmic portion of the electrode impedance and includes contributions from the electronic conductivity of the electrodes and ionic conductivity of the electrolyte solution, as well as any electronic contact resistances associated with the cell hardware, current collectors, and electrode materials[26,27]. The high frequency depressed semicircles (100 kHz to 200 mHz) are generally associated with interfacial impedance due to SEI formation[28] and the interphase electronic contacts between the current collector and conductive additive/binder system as described in by Gaberscek, et al.[29,30] Each of these arcs can be associated with a separate interfacial phenomenon whose time constant corresponds to the frequency at which the peak of the depressed semicircle is situated[26]. The high-frequency depressed semicircle in this work corresponds to the combined impedance of the SEI film and contact interface among the current collector and active material (CPE$_{sei + int}$ and R$_{sei + int}$)[9,31]. The depressed semicircle in the medium-frequency region contains information about charge-transfer resistance (R_{CT}) and W_O, the circuit element responsible for the low-frequency (<200 mHz) Warburg impedance tail, which describes diffusion-related phenomena in the device[32]. This includes the diffusion of salt in the electrolyte and diffusion of Liions into the bulk of the active material[26,27]. Previous research has shown that interfacial effects of the negative electrode are dominated by kinetics, while the positive electrode exhibits a diffusion-dominated behavior[26]. This explains the relatively shorter tail in the impedance spectrum of our anode.
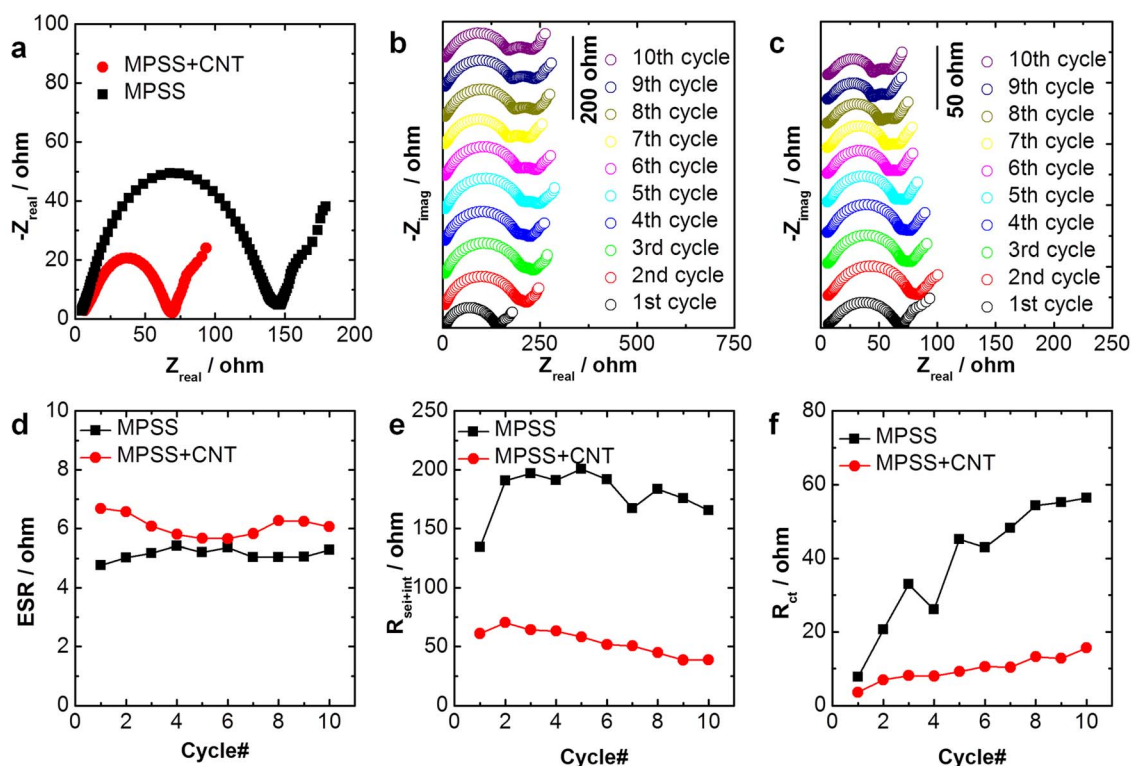
Figure 5 | (a) Nyquist plots of MPSS based LIB cells with and without the CNT additive. (b) Nyquist plots of the MPSS electrodes (with carbon black) and (c) MPSS-CNT anodes (with 2 wt.% CNTs) over 10 charge-discharge cycles. (d) Equivalent series resistance, (e) SEI and interphase electronic contact resistance, and (f) charge transfer resistance as a function of cycling number.

The first cycle EIS plots are shown in Fig. 5a. while the apparent ESR is similar for both systems, it is noteworthy that MPSSs with CNTs demonstrate a slightly smaller value and exhibit approximately half as much interphase electronic contact resistance plus SEI resistance as that of MPSSs with carbon black (demonstrated by the diameter of the first semicircle). To better understand the EIS evolution and capacity fading mechanism of these two systems, EIS measurements were performed over 10 consecutive cycles for both systems, as in Fig. 5b and 5c. Based on the behavior of the Nyquist spectra and previous studies, the equivalent circuit for our MPSS-based electrode system is shown in Fig. S2a[33,34]. The fitted impedance parameters including ESR, $R_{sei+int}$, and the Rct at different cycles are summarized in Fig. 5d, 5e and 5f and experimental and fitted EIS plots are summarized in Fig. S2b. Both systems exhibited low and stable ESR values with a small range of fluctuations (5.5 ± 1 ohm) in the first 10 cycles. The $R_{sei+int}$ for both systems increases in the first two cycles and it tends to stablize and then gradually decrease afterwards. The increase in the second cycle can be atributed to the continuous formation of SEI layer. Since the electrodes are pressed by a spring in coin cell configuration, the decrease of $R_{sei+int}$ may due to the irreversible electrode volume during cycling which results in gradually increasing of the pressure on the electrodes. Therefore, the interphase electronic contact resistance was slightly improved. It is worth noting that the MPSS electrodes with 2 w.t% CNT additive demonstrate ~60% lower $R_{sei+int}$ compared with MPSS electrodes with carbon black only, which further confirms the effectiveness of using CNTs as condutive additive for nanosilicon materials. R_{ct} values for MPSS electrodes with carbon black only increase constantly (over 10 times) over the first 10 cycles while the R_{ct} of electrodes based on MPSS with 2 wt.% CNTs tends to stabilize at ~10 ohm. Since the charge transfer reaction primarily happens on the surface of the MPSSs, the electronic contact between MPSSs and conductive additives/binders has a great impact on the charge transfer reaction. Comparing the electrodes with CNT to

without CNT additive, the addition of CNTs provides an interpenetrating conductive network within the composite electrode which facilitates charge transfer and minimizes the degradation of the electronic contact between MPSSs and conductive additives/binder. The low frequency tails, representing diffusion impedance, are shorter for the system with CNTs thereby implying faster and more facile diffusion of Li-ions into the electrode.

In summary, we have reported the synthesis of highly monodisperse porous silicon spheres (MPSSs) via a facile hydrolysis process with subsequent surface-protected magnesiothermic reduction. The spherical nature of the monodisperse porous nanospheres permits a homogeneous stress-strain distribution within the structure during lithiation and delithiation. We have also shown the Li-ion battery anodes based on MPSSs demonstrate a high reversible capacity of ~3105 mAh g^{-1}, superior rate performance, and excellent cycling stability.

Methods

Materials synthesis. Monodisperse solid silica spheres (SS) are prepared via the modified Stober method[19]. Firstly, 9 ml NH_3H_2O, 16.25 ml ethanol, and 24.75 ml DI water are premixed under room temperature while stirring at 1100 rpm to form a uniform mixture solution A. Next, solution B is prepared by adding 4.5 ml TEOS to 45.5 ml ethanol. Solution B is added into the mixture solution A while stirring at 450 rpm and the final mixture is kept stirring for 2 hours. The final products are washed with a mixture of water and ethanol repeatedly and collected by centrifuging and vacuum drying.

SiO_2 nanosphere powder is mixed with NaCl (>99.5%, Fisher Scientific) in a 1 : 10 w/w ratio and milled in an alumina mortar. The SiO_2:NaCl powder is immersed in DI H_2O and ultrasonicated for 1 hour and subsequently vigorously stirred at 50°C for 3 hours. The solution is dried at 90°C under vacuum to remove all water. The resulting SiO_2:NaCl powder is then mixed with Mg (99.5%, −325 mesh, Sigma-Aldrich) in a 1 : 0.9 w/w SiO_2:Mg ratio. After vortexing the powder for ample mixing, the powder is loaded into SS 316 Swagelok-type reactors in an argon-filled VAC Omni-lab glovebox (0.5 ppm H_2O, <0.1 ppm O_2). The reactors are loaded into an MTI GSL-1200X quartz tube furnace and purged with argon. The furnace is heated to 700°C at a rate of 5°C/min, held for 6 hours, and cooled to room temperature. The resulting product is then washed with DI H_2O several times to remove NaCl. Unwanted Mg_2Si and MgO is removed via etching in concentrated HCl overnight

with subsequent washing with DI H_2O. Unreacted SiO_2 is removed by etching in 5% HF for 1 hour. The powder is rinsed several times with DI H_2O, dispersed in ethanol, and ultimately dried under vacuum for 4 hours at 100°C.

Materials characterization. The surface morphology is investigated using optical microscopy, scanning electron microscopy (SEM; leo-supra, 1550) with an X-ray energy-dispersive spectroscopy (EDS), and transmission electron microscopy (TEM; Philips, CM300) with a LaB_6 cathode operated at 300 KV. For TEM imaging, the sample is ultrasonically dispersed in ethanol for 1 hr and then diluted and dropped onto a TEM grid. A Renishaw DXR Raman spectroscopy system with a 532 nm laser (8 mW excitation power, 100× objective lens) source is used to characterize SS and MPSS.

Fabrication and testing of lithium ion battery (LIB). The electrodes were prepared by casting a slurry containing 70% active material (SS, MPSS, or C-MPSS in this work), 20% conductive additive (carbon black), and 10% sodium alginate binder. The per-area mass loading for the as-prepared electrodes were 0.5–1.0 mgcm^{-2}. A button-type (CR 2032) two-electrode half-cell configuration was used for the electrochemical measurements. The LIBs were assembled in an Ar filled glovebox with moisture and oxygen level below 1 ppm. Pure lithium metal was used as the counter electrode of the LIB. A porous membrane (Celgard 3501) was used as the separator. In this work, 1 M $LiPF_6$ dissolved in a 1 : 1 (v : v) mixture of ethylene carbonate (EC) and dimethyl carbonate (DMC) was used as the electrolyte. Cyclic voltammetry scans were performed with a voltage window range of 0.01 to 2.0 V (vs. Li^+/Li) at a scan rate of 0.2 mV sec^{-1}. Galvanostatic charge-discharge and cycling performance measurements were conducted at a fixed voltage window between 0.01 V and 2.0 V (vs. Li^+/Li). The C rate was defined based on the theoretical Li storage capacity of Si which is ~3579 mAh g^{-1} for $Li_{15}Si_4$ at room temperature[12,35]. Electrochemical impedance spectroscopy (EIS) was conducted to evaluate the charge transfer performance of the LIBs. Potentiostatic EIS measurements were performed between 0.01 Hz and 1 MHz with an amplitude of 10 mV.

1. Chan, C. K. et al. High-performance lithium battery anodes using silicon nanowires. Nat. Nanotechnol. **3**, 31–35 (2007).
2. Liu, N. et al. A pomegranate-inspired nanoscale design for large-volume-change lithium battery anodes. Nat. Nanotechnol. **9**, 187–192 (2014).
3. Wang, W. et al. Hydrous Ruthenium Oxide Nanoparticles Anchored to Graphene and Carbon Nanotube Hybrid Foam for Supercapacitors. Sci. Rep. **4** (2014).
4. Wang, W., Guo, S., Bozhilov, K. N., Yan, D., Ozkan, M. & Ozkan, C. S. Intertwined Nanocarbon and Manganese Oxide Hybrid Foam for High-Energy Supercapacitors. Small **9**, 3714–3721 (2013).
5. Wang, W. et al. Three dimensional few layer graphene and carbon nanotube foam architectures for high fidelity supercapacitors. Nano Energy **2**, 294–303 (2013).
6. Wang, W. et al. Hybrid Low Resistance Ultracapacitor Electrodes Based on 1-Pyrenebutyric Acid Functionalized Centimeter-Scale Graphene Sheets. J. Nanosci. Nanotechnol. **12**, 6913–6920 (2012).
7. Wang, W., Guo, S., Ozkan, M. & Ozkan, C. S. Chrysanthemum like carbon nanofiber foam architectures for supercapacitors. J. Mater. Res. **28**, 912–917 (2013).
8. Favors, Z. et al. Scalable Synthesis of Nano-Silicon from Beach Sand for Long Cycle Life Li-ion Batteries. Sci. Rep. **4**, 1–7, doi:10.1038/srep05623 (2014).
9. Wang, W. et al. Silicon Decorated Cone Shaped Carbon Nanotube Clusters for Lithium Ion Battery Anodes. Small **10**, 3389–3396 (2014).
10. Wang, W. et al. Hybrid carbon nanotube and graphene nanostructures for lithium ion battery anodes. Nano Energy **3**, 113–118 (2014).
11. Ge, M., Rong, J., Fang, X., Zhang, A., Lu, Y. & Zhou, C. Scalable preparation of porous silicon nanoparticles and their application for lithium-ion battery anodes. Nano Res. **6**, 174–181 (2013).
12. Liu, X. H., Zhong, L., Huang, S., Mao, S. X., Zhu, T. & Huang, J. Y. Size-Dependent Fracture of Silicon Nanoparticles During Lithiation. ACS Nano **6**, 1522–1531 (2012).
13. McDowell, M. T. et al. In Situ TEM of Two-Phase Lithiation of Amorphous Silicon Nanospheres. Nano Lett. **13**, 758–764 (2013).
14. Wu, H., Zheng, G., Liu, N., Carney, T. J., Yang, Y. & Cui, Y. Engineering empty space between Si nanoparticles for lithium-ion battery anodes. Nano Lett. **12**, 904–909 (2012).
15. Wu, H. et al. Stable cycling of double-walled silicon nanotube battery anodes through solid-electrolyte interphase control. Nat. Nanotechnol. **7**, 310–315 (2012).
16. Yu, C. et al. Silicon Thin Films as Anodes for High-Performance Lithium-Ion Batteries with Effective Stress Relaxation. Adv. Energy Mater. **2**, 68–73 (2012).
17. Kim, H., Han, B., Choo, J. & Cho, J. Three-Dimensional Porous Silicon Particles for Use in High-Performance Lithium Secondary Batteries. Angew. Chem. Int. Ed. **120**, 10305–10308 (2008).
18. Ge, M., Rong, J., Fang, X. & Zhou, C. Porous doped silicon nanowires for lithium ion battery anode with long cycle life. Nano Lett. **12**, 2318–2323 (2012).
19. Stöber, W., Fink, A. & Bohn, E. Controlled growth of monodisperse silica spheres in the micron size range. J. Colloid Interface Sci. **26**, 62–69 (1968).
20. Luo, W. et al. Efficient Fabrication of Nanoporous Si and Si/Ge Enabled by a Heat Scavenger in Magnesiothermic Reactions. Sci. Rep. **3**, 1–7, doi:10.1038/srep02222 (2013).
21. Kovalenko, I. et al. A major constituent of brown algae for use in high-capacity Li-ion batteries. Science **334**, 75–79 (2011).
22. Yan, N. et al. Hollow Porous SiO_2 Nanocubes Towards High-performance Anodes for Lithium-ion Batteries. Sci. Rep. **3**, 1–6, doi:10.1038/srep01568 (2013).
23. Favors, Z., Wang, W., Bay, H. H., George, A., Ozkan, M. & Ozkan, C. S. Stable Cycling of SiO_2 Nanotubes as High-Performance Anodes for Lithium-Ion Batteries. Sci. Rep. **4**, 1–7, doi:10.1038/srep04605 (2014).
24. Baggetto, L., Niessen, R. A., Roozeboom, F. & Notten, P. H. High Energy Density All-Solid-State Batteries: A Challenging Concept Towards 3D Integration. Adv. Funct. Mater. **18**, 1057–1066 (2008).
25. Welna, D. T., Qu, L., Taylor, B. E., Dai, L. & Durstock, M. F. Vertically aligned carbon nanotube electrodes for lithium-ion batteries. J. Power Sources **196**, 1455–1460 (2011).
26. Dees, D., Gunen, E., Abraham, D., Jansen, A. & Prakash, J. Alternating current impedance electrochemical modeling of lithium-ion positive electrodes. J. Electrochem. Soc. **152**, A1409–A1417 (2005).
27. Wang, G., Yang, L., Chen, Y., Wang, J., Bewlay, S. & Liu, H. An investigation of polypyrrole-LiFePO$_4$ composite cathode materials for lithium-ion batteries. Electrochim. Acta **50**, 4649–4654 (2005).
28. Barsoukov, E., Kim, J. H., Kim, J. H., Yoon, C. O. & Lee, H. Effect of Low-Temperature Conditions on Passive Layer Growth on Li Intercalation Materials In Situ Impedance Study. J. Electrochem. Soc. **145**, 2711–2717 (1998).
29. Gaberscek, M., Moskon, J., Erjavec, B., Dominko, R. & Jamnik, J. The importance of interphase contacts in Li ion electrodes: the meaning of the high-frequency impedance arc. Electrochem. Solid-State Lett. **11**, A170–A174 (2008).
30. Guo, J., Sun, A., Chen, X., Wang, C. & Manivannan, A. Cyclability study of silicon–carbon composite anodes for lithium-ion batteries using electrochemical impedance spectroscopy. Electrochim. Acta **56**, 3981–3987 (2011).
31. Hu, L., Zhong, H., Zheng, X., Huang, Y., Zhang, P. & Chen, Q. CoMn$_2O_4$ spinel hierarchical microspheres assembled with porous nanosheets as stable anodes for lithium-ion batteries. Sci. Rep. **2**, 1–8, doi:10.1038/srep00986 (2012).
32. Wang, X. et al. TiO2 modified FeS Nanostructures with Enhanced Electrochemical Performance for Lithium-Ion Batteries. Sci. Rep. **3**, 1–8, doi:10.1038/srep02007 (2013).
33. Guo, J., Chen, X. & Wang, C. Carbon scaffold structured silicon anodes for lithium-ion batteries. J. Mater. Chem. **20**, 5035–5040 (2010).
34. Liu, P. & Wu, H. Construction and destruction of passivating layer on Li$_x$C$_6$ in organic electrolytes: an impedance study. J. Power Sources **56**, 81–85 (1995).
35. Kasavajjula, U., Wang, C. & Appleby, A. J. Nano-and bulk-silicon-based insertion anodes for lithium-ion secondary cells. J. Power Sources **163**, 1003–1039 (2007).

Author contributions

Additional information

Supplementary information accompanies this paper at http://www.nature.com/scientificreports

Competing financial interests: The authors declare no competing financial interests.

How to cite this article: Wang, W. et al. Monodisperse Porous Silicon Spheres as Anode Materials for Lithium Ion Batteries. Sci. Rep. **5**, 8781; DOI:10.1038/srep08781 (2015).